

Experimental study on seismic performance of steel reinforced concrete T-shaped columns

Zuqiang Liu^{*1,2}, Chaofeng Zhou^{1,3}, Jianyang Xue^{1,2} and Roberto T. Leon⁴

¹School of Civil Engineering, Xi'an University of Architecture and Technology, Xi'an 710055, China

²Key Lab of Structural Engineering and Earthquake Resistance, Ministry of Education (XAUAT), Xi'an 710055, China

³Henan University of Technology, Zhengzhou 450001, China

⁴Department of Civil and Environmental Engineering, Virginia Tech, Blacksburg 24060, USA

(Received November 8, 2019, Revised July 8, 2020, Accepted July 9, 2020)

Abstract. This study investigates the seismic performance of steel reinforced concrete (SRC) T-shaped columns under low cyclic loading tests. Based on test results of ten half-scale column specimens, failure patterns, hysteretic behavior, skeleton curves, ultimate strength, ductility, stiffness degradation and energy dissipation capacity were analyzed. The main variables included loading angles, axial compression ratios and steel ratios. The test results show that the average values of the ductility factor and the equivalent viscous damping coefficient with respect to the failure of the columns were 5.23 and 0.373, respectively, reflecting good seismic performance. The ductility decreased and the initial stiffness increased as the axial compression ratio of the columns increased. The strength increased with increasing steel ratio, as expected. The columns displaced along the web had higher strength and initial stiffness, while the columns displaced along the flange had better ductility and energy dissipation capacity. Based on the test and analysis results, a formula is proposed to calculate the effective stiffness of SRC T-shaped columns.

Keywords: steel reinforced concrete; T-shaped column; seismic performance; cyclic loading; effective stiffness

1. Introduction

A special-shaped column is a column with an L-shaped, T-shaped or cross-shaped section, located at the intersection of the main structural system lines (Fig. 1). These columns, which maintain the same thickness as the main walls, can not only save space but also provide a full rectangular space without column penetrations at the corners (Abo-Zai *et al.* 2019, Nzabonimpa and Hong 2018). In last few decades, reinforced concrete (RC) special-shaped columns (Fig. 2) have been extensively studied. Most work focused on computer calculation methods for strength under biaxial eccentric compression (Ramamurthy and Khan 1983, Hsu 1989, Tsal and Hsu 1993), as well as experimental work on seismic performance (Li *et al.* 2002, Pham and Li 2015). However, due to the lower stiffness and ductility (Xiao *et al.* 2011, Liu *et al.* 2016), RC special-shaped columns have been found limited practical application.

Steel and concrete composite structural members have been shown to provide high axial and flexural capacity and good seismic performance (Kara *et al.* 2015, Montava *et al.* 2019, Lai *et al.* 2019), and have been extensively employed in tall buildings, particularly in the earthquake-prone regions. Considering the advantages of composite structural members, some researchers have proposed steel and concrete composite special-shaped columns (Kim *et al.*

2012, Tokgoz and Dundar 2012, Kim *et al.* 2014, Patton and Singh 2017) as a better structural alternative, in which steel reinforced concrete (SRC) special-shaped column is reinforced with steel, longitudinal rebars and transverse stirrups in the special-shaped section (Fig. 3).

The SRC T-shaped column, which is usually used as exterior column and which is potentially the most attractive of SRC special-shaped columns, has not been the object of extensive studies. Based on cyclic loading tests on nine specimens of SRC T-shaped columns, the design limit values for axial compression ratio under different seismic demand levels was put forward by Chen *et al.* (2016). However, it is clear from those investigations that several important topics on the seismic performance of SRC T-shaped column have not been fully addressed and that little or no research has addressed the calculation of the effective stiffness of SRC T-shaped columns.

In this study, ten SRC T-shaped columns with shear span ratio of 2.5 were fabricated and subjected to low cyclic loading tests. The observed failure patterns, hysteretic loops, skeleton curves, ductility, stiffness degradation and energy dissipation capacity of these SRC T-shaped columns are discussed in this paper. The influence of design parameters (i.e., loading angles, axial compression ratios and steel ratios) on the seismic performance of SRC T-shaped column are analyzed in detail. Furthermore, a calculation method of effective stiffness for SRC T-shaped column is proposed.

*Corresponding author, Associate Professor
E-mail: liuzuqiang@xauat.edu.cn

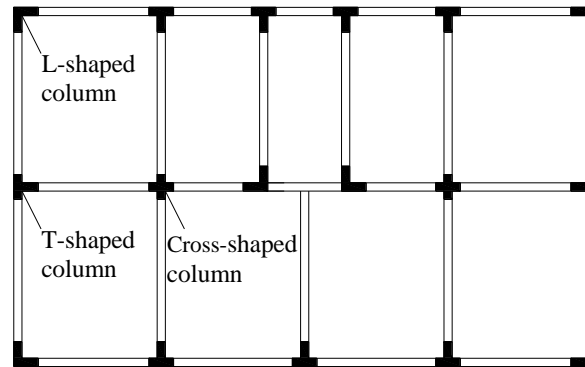


Fig. 1 Plan of a typical structure with special-shaped columns

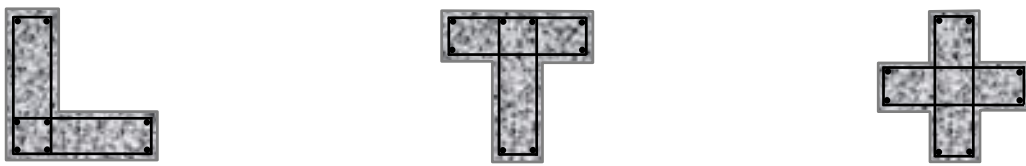


Fig. 2 Typical RC special-shaped column sections

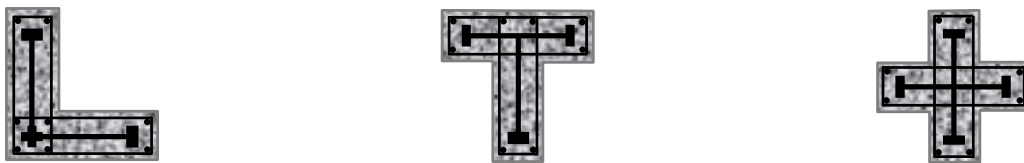


Fig. 3 Typical SRC special-shaped column sections

Table 1 Design parameters of SRC T-shaped columns

Specimen no.	Loading angle	n	ρ_{ss}
TW1	Along web	0.4	7.09%
TW2	Along web	0.2	7.09%
TW3	Along web	0.6	7.09%
TW4	Along web	0.4	6.18%
TW5	Along web	0.4	8.01%
TF1	Along flange	0.4	7.09%
TF2	Along flange	0.2	7.09%
TF3	Along flange	0.6	7.09%
TF4	Along flange	0.4	6.18%
TF5	Along flange	0.4	8.01%

2. Experimental program

2.1 Specimen design

Ten half-scale SRC T-shaped columns with limb thickness of 120mm and sectional depth-thickness ratio of 3 were designed and constructed for these experiments. The design variables were the loading angle (TW=along web, TF=along flange), axial compression ratio ($n=0.2, 0.4$ and

0.6) and steel ratio ($\rho_{ss}=6.18\%, 7.09\%$ and 8.01%), as presented in Table 1 and Fig. 4. Dimension and reinforcing details are given in Fig. 5. The shear-span ratio of the specimens was 2.5.

2.2 Fabrication and material properties

All the columns were reinforced with solid-web steel plates, eight longitudinal rebars and transverse stirrups with

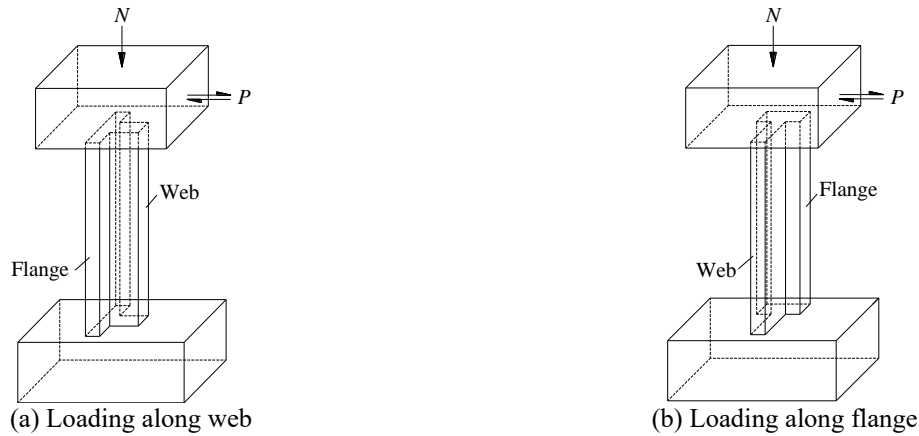


Fig. 4 Definition of loading angle

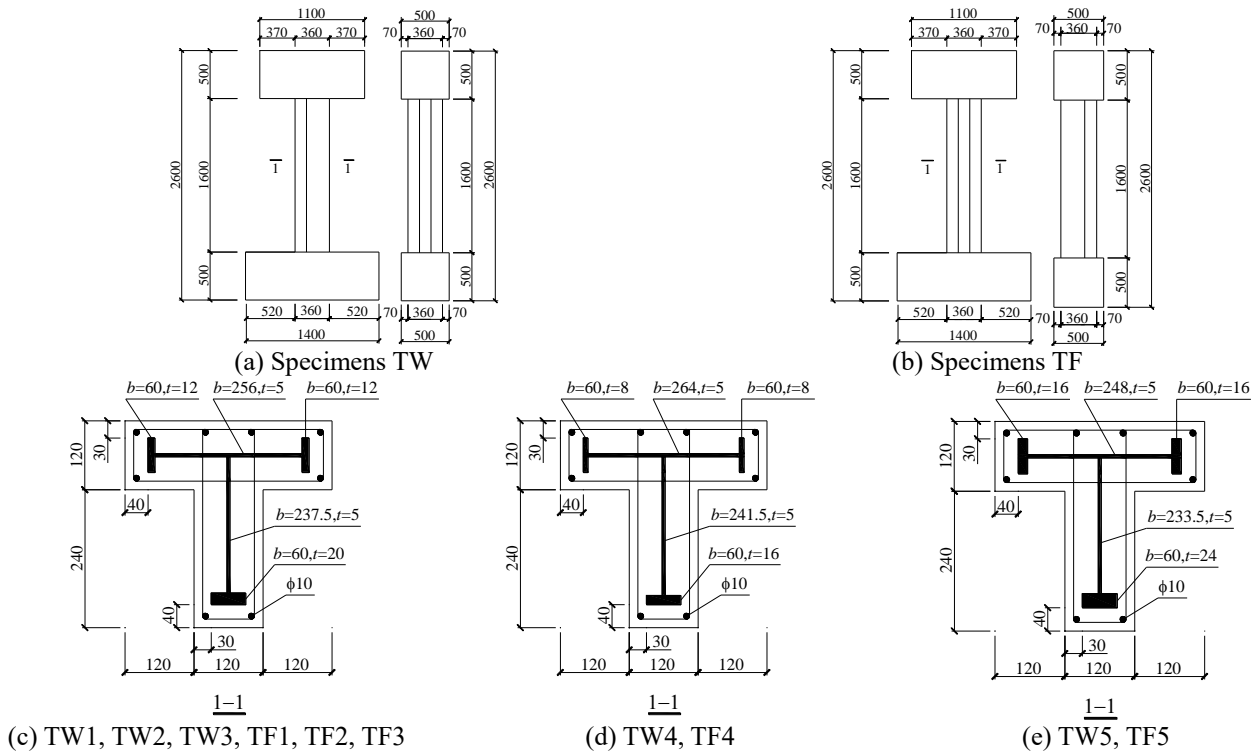


Fig.5 Detailed dimensions of specimens

a spacing of 60 mm. Steel plates with different thicknesses were welded together to form solid-web steel (Fig. 6); the structural steel was Q235 (about equivalent to ASTM A36). The U-shaped or closed rectangular-shaped transverse stirrups ($\Phi 6$) were welded on the solid-web steel, and the longitudinal rebars ($\Phi 10$) were assembled with stirrups (Fig. 7). The ratio of longitudinal rebars and transverse stirrups for all the columns were 0.873% and 1.41%, respectively. The mechanical properties of steel plates and rebars obtained from the material property tests are given in Table 2.

Commercial concrete with aggregate diameter of 2.5~5 mm was adopted to cast the columns. Concrete cubes ($150 \times 150 \times 150 \text{ mm}^3$) made at the time of concrete casting

were tested to determine the concrete properties. Average cube compressive strengths on the 28th day were 34.5MPa for specimens TW and 33.6MPa for specimens TF.

2.3 Test setup and procedure

The cyclic loading tests were performed using a multi-functional electro-hydraulic servo test machine in the Key Laboratory of Structural Engineering at X'an University of Architecture and Technology, China. In order to simulate the boundary conditions of actual structures more accurately, a Kenken device was adopted in the test set-up for the cyclic loading tests, as shown in Fig. 8. The top foundation beam of the SRC columns was connected to the Kenken

Table 2 Mechanical properties of steel plates and rebars

Specimen	Material	Thickness or Diameter	Yield strength (MPa)	Ultimate strength (MPa)	Elastic modulus (MPa)
Specimens TW	Steel plates	5 mm	321.0	475.1	2.13×10^5
		8 mm	306.8	468.9	1.93×10^5
		12 mm	298.5	432.2	2.11×10^5
		16 mm	285.0	445.6	2.04×10^5
		20 mm	279.6	412.7	1.99×10^5
	24 mm	269.3	412.7	1.98×10^5	
	Rebars	10 mm	369.0	518.7	2.10×10^5
Specimens TF	Steel plates	5 mm	253.0	390.2	2.14×10^5
		8 mm	291.6	391.3	2.11×10^5
		12 mm	294.2	403.9	2.07×10^5
		16 mm	258.3	397.9	1.94×10^5
		20 mm	209.9	350.0	1.98×10^5
	24 mm	205.9	343.6	1.97×10^5	
	Rebars	10 mm	417.0	553.3	2.11×10^5



Fig. 6 Solid-web steel



Fig. 7 Complete steel skeleton

device and the bottom foundation beam was fixed to the laboratory floor. The specimens were restrained against out-of-plane torsion.

All the columns were subjected to an axial compression force while undergoing cyclic lateral displacements. The force diagram is presented in Fig. 9. Initially, the axial compression force was applied on the top surface of the top foundation beam using a 2000 kN hydraulic jack. After the axial compression force stabilised, the cyclic lateral loads were applied at the height of the column inflection point using a 1000 kN MTS electro-hydraulic servo machine.

The loading procedure for the cyclic lateral loads is shown in Fig. 10, and it involved two load stages: an initial force-controlled stage and a latter displacement-controlled stage. In the load-controlled stage, increments of 20 kN of the lateral load were imposed until the column yielded. Subsequently, the loading procedure was changed into a displacement-controlled stage with increments of the displacement in multiples of Δ_y , the yield displacement. Each displacement level was repeated thrice until the lateral load of the columns dropped below the 85% peak value.

2.4 Measuring devices

The positions of linear variable differential transducers (LVDTs) on the SRC T-shaped columns are shown in Fig. 11. LVDT-1 and LVDT-2 were installed to monitor the in-plane lateral displacement of the load point and the inflection point of the SRC T-shaped columns, respectively. LVDT-3 was installed to monitor any lateral slip of the bottom foundation beam. Based on the LVDT-3 reading, the lateral displacement of the load point and inflection point could be adjusted.

The strains of the solid-web steel and longitudinal rebars at both column ends were measured using foil strain gages.

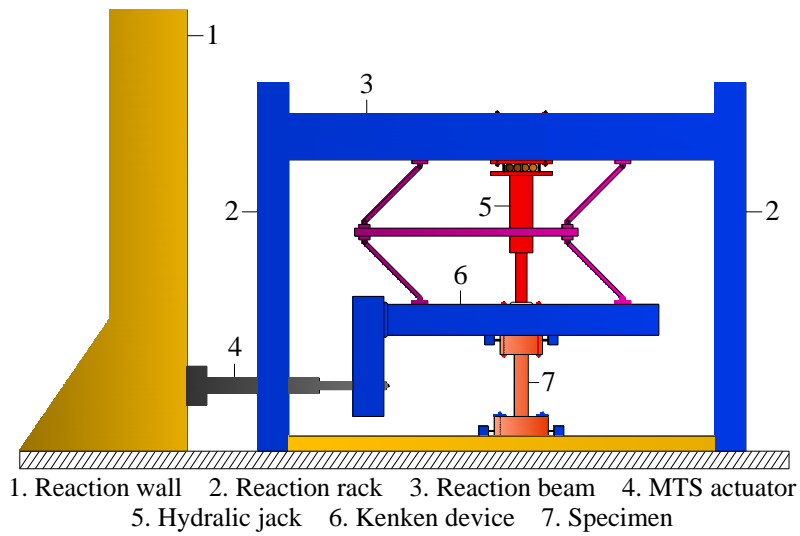


Fig. 8 Test set-up

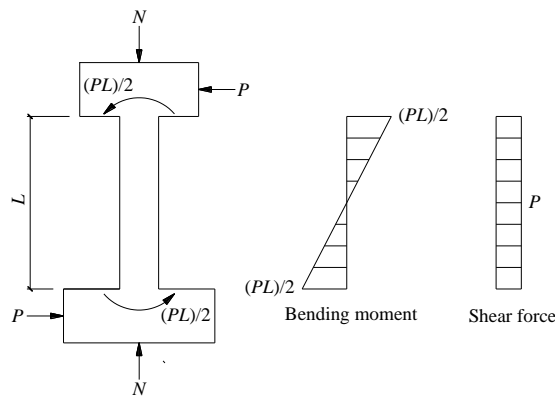


Fig. 9 Force diagram for SRC T-shaped column

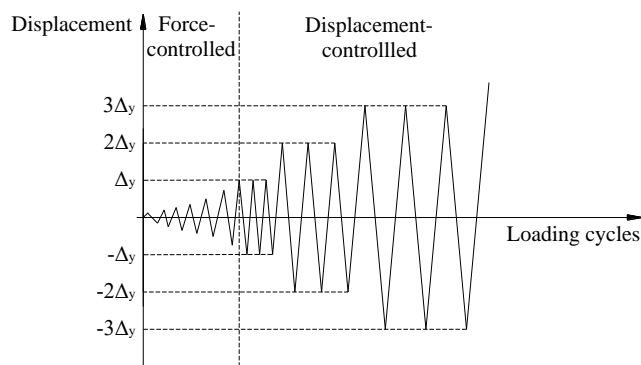


Fig. 10 Loading procedure

The gages were located 30 mm below the bottom surface of the top foundation beam and above the top surface of the bottom foundation beam, respectively, at the locations shown in Fig. 12.

3. Experimental results and discussion

3.1 General behavior

Fig. 13 illustrates the appearance of the SRC T-shaped columns at the end of loading tests. All column specimens

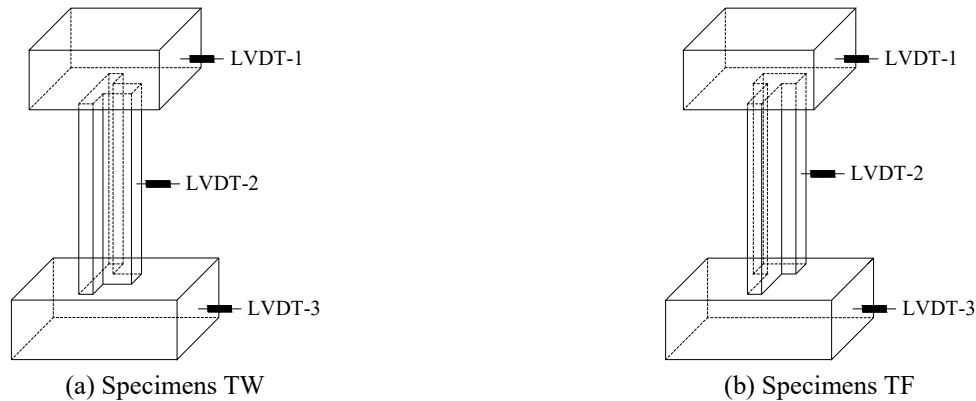


Fig. 11 Installation position of LVDTs



Fig. 12 Measurement points of strains for solid-web steel and longitudinal rebars

experienced flexural failures, with the solid-web steel and longitudinal rebars yielding prior to concrete crushing. However, because of different loading angles, the failure patterns of specimens TW and specimens TF were different.

3.1.1 Specimens TW

For specimens TW (Figs. 13(a) to 13(e)), the web at both column ends was the main damaged region. As shown in Fig. 14(a), the cross section of the columns was unsymmetrical with respect to the centroid axis along the loading direction, with the area of concrete and steel in tension and compression on the web being smaller than that on the flange. Therefore, under cyclic lateral loads, the concrete on the web cracked and crushed earlier than the concrete on the flange, respectively. At the end of loading, large portions of the concrete on the web spalled off and the steel on the web yielded in both tension and compression. On the other hand, the concrete on the flange had just begun to crush and spall off and the steel on the flange only yielded in tension.

3.1.2 Specimens TF

For specimens TF (Figs. 13(f) to 13(j)), the flanges at both column ends were the main damaged regions. As shown in Fig. 14(b), the cross section of the columns was symmetrical with respect to the centroidal axis along the loading direction, with the web located near the neutral axis. Therefore, under cyclic lateral loads, both sides of the flange alternated in tension and compression, but the web hardly participated in resisting the load. At the end of

loading, the concrete on both sides of the flange spalled off severely and the steel on both sides of the flange yielded in tension and compression. By contrast, there was no concrete crushing and steel yielding on the web, and only some vertical bond cracks on the web were observed.

3.2 Load-displacement curve

Fig. 15 shows the lateral load-lateral displacement hysteresis of the columns. Based on these plots, the following observations can be made:

(1) The spindle-shaped loops indicate good energy dissipation capacity for all specimens. In the uncracked stage, there was a linear relationship between load and displacement with the loading and unloading paths coinciding. As behavior shifted into the inelastic stage, cracks appeared at both ends of the columns. At this point the slopes of the hysteretic loops began to decrease, and a larger residual deformation was observed when the lateral load was removed. After the lateral load reached the peak value, the strength and stiffness degeneration became more and more obvious with the increase of the lateral displacement from $1\Delta_y$ to $3\Delta_y$.

(2) For the columns subjected to the same loading angle, the larger the axial compression ratio was, the narrower the hysteretic loops became and the more quickly the lateral load declined after it reached the peak value. As the steel ratio increased, both the area of one hysteretic loop at the same level of lateral load (displacement) and the number of loops before columns failed increased.

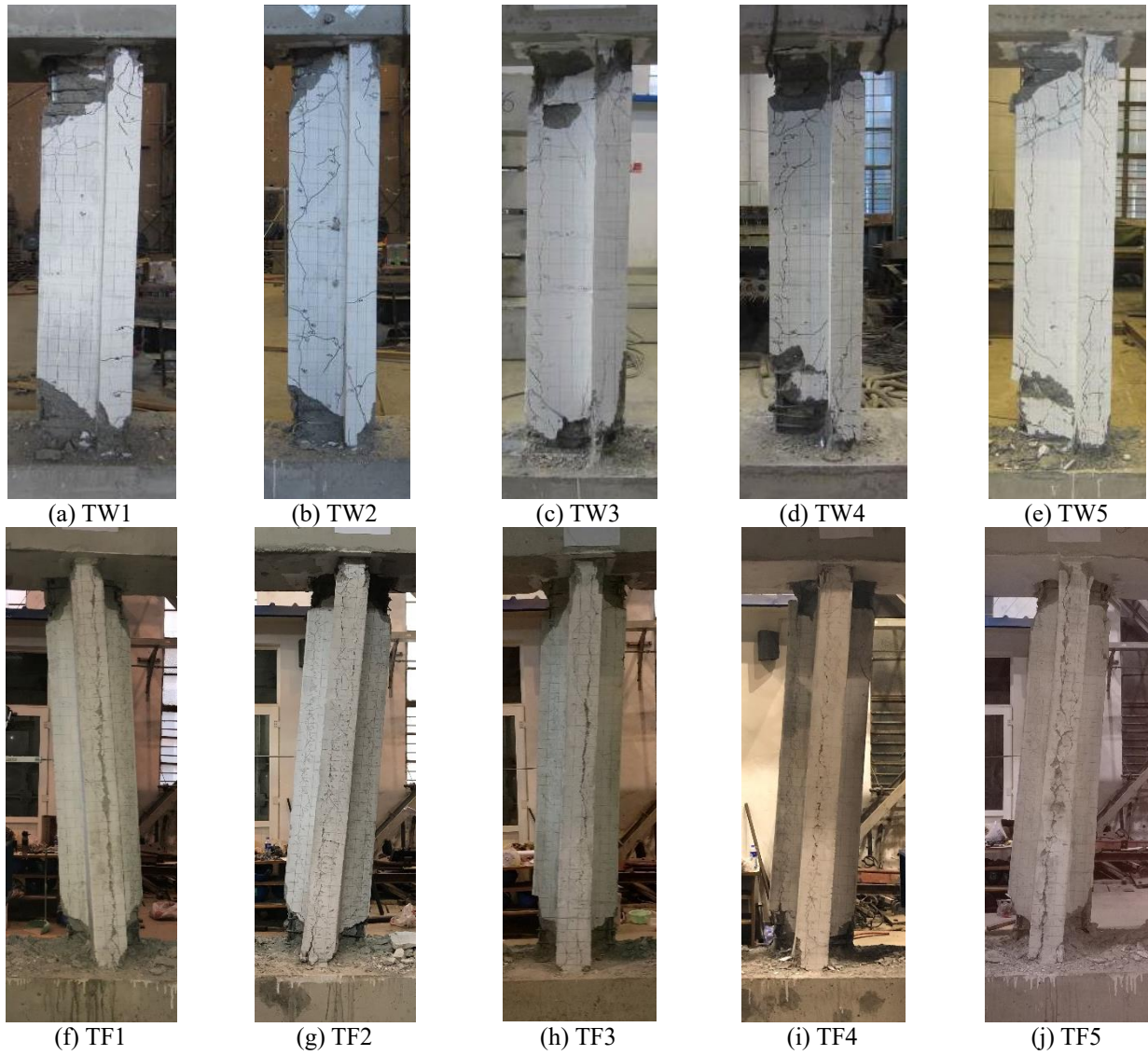


Fig. 13 Failure patterns of specimens



Fig. 14 Difference of cross section under different loading angles

(3) For the columns subjected to the same axial compression ratio and steel ratio, the maximum load of the specimen TW was larger than that of the specimen TF. In contrast, the displacement corresponding to the maximum load of the specimen TW was smaller than that of the specimen TF. The hysteretic loops of specimen TW were

somewhat narrower than that of specimen TF at the same level of lateral load (displacement).

The skeleton curves of all the SRC T-shaped columns are plotted in Fig. 16. From the skeleton curves, three critical characteristic points, namely, a yield point (P_y, Δ_y), an ultimate point (P_u, Δ_u) and a failure point (P_f, Δ_f) can be

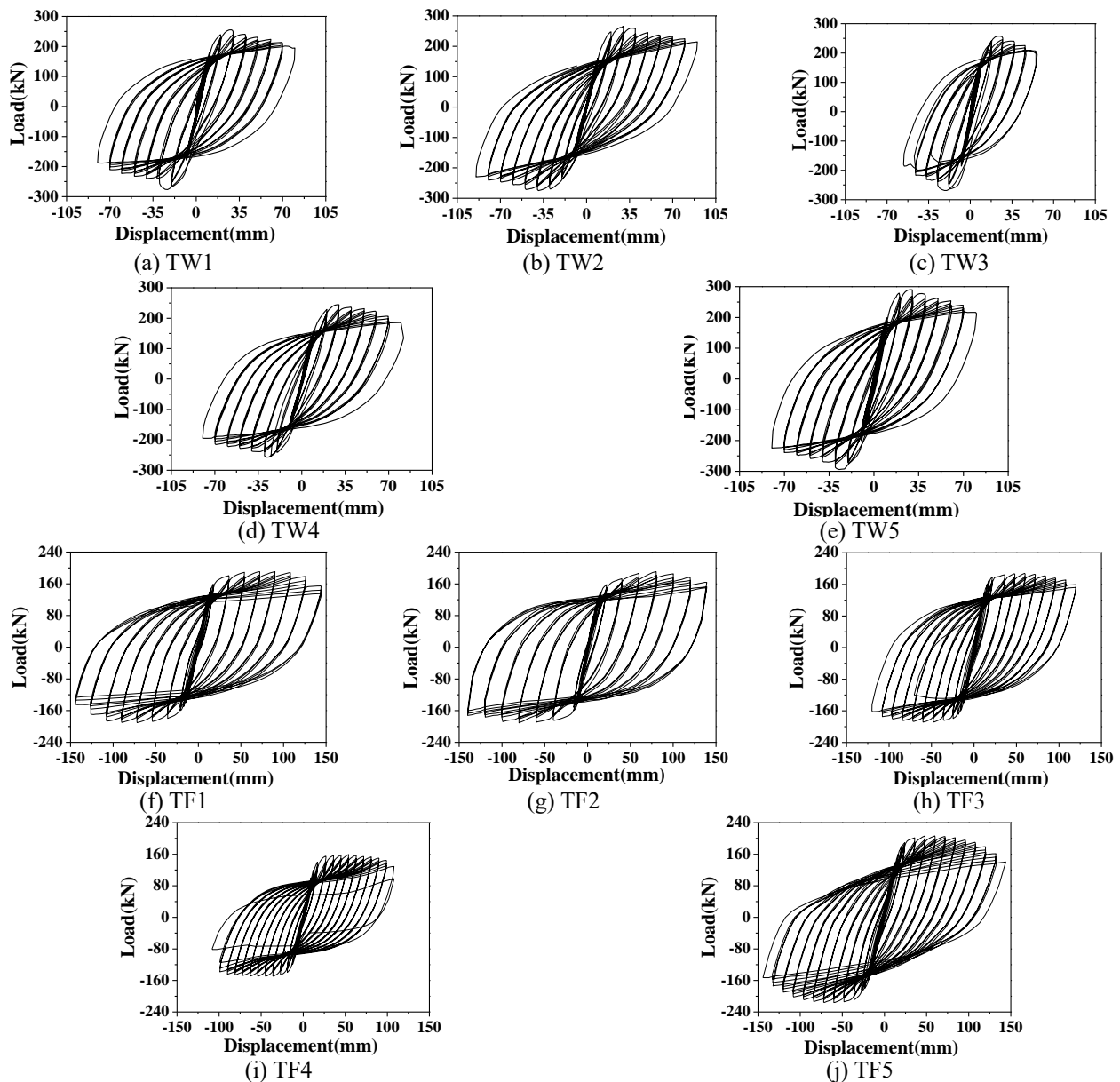


Fig. 15 Hysteretic loops

obtained. The loads and displacements corresponding to these three points are listed in Table 3. The yield point can be determined using a graphical method (Nie *et al.* 2008). The ultimate load and the failure load are selected as the maximum load and 85% of the maximum load in the downward section of skeleton curve, respectively.

3.3 Characteristic loads

Table 3 lists the characteristic loads of all specimens, namely, yield loads P_y , ultimate loads P_u and failure loads P_f . Fig. 17 shows the influences of design parameters on the columns' average ultimate loads in the pull and push directions. Table 3 and Fig.17 together show the following:

(1) For the columns subjected to the same loading angle and steel ratio, with the axial compression ratio

increasing from 0.2 to 0.6, the average of yield loads, ultimate loads and failure loads were almost the same. This indicates that the axial compression ratio from 0.2 to 0.6 did not significantly influence the characteristic loads of the SRC T-shaped column.

(2) For the columns subjected to the same loading angle and axial compression ratio, the yield loads, ultimate loads and failure loads increased significantly as the steel ratio increased. This suggests that increasing the steel ratio improves the ultimate capacity of the SRC T-shaped column.

(3) For the columns subjected to the same axial compression ratio and steel ratio, the yield loads, ultimate loads and failure loads of specimen TW were much larger than that of specimen TF, respectively. It is because the area of concrete and steel near the neutral axis for specimen TF,

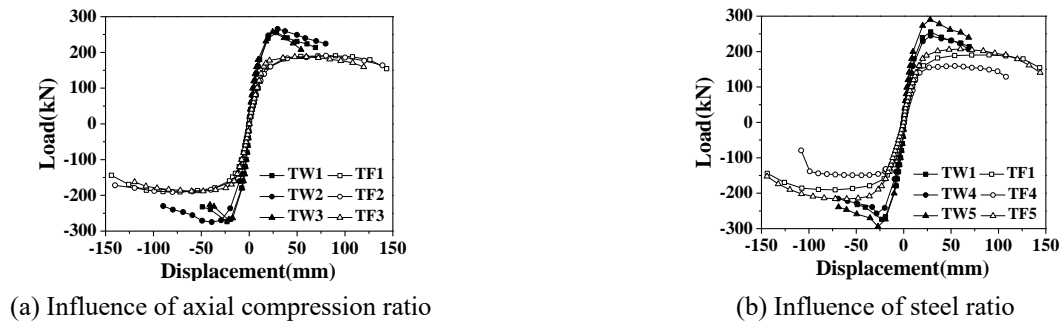


Fig. 16 Skeleton curves

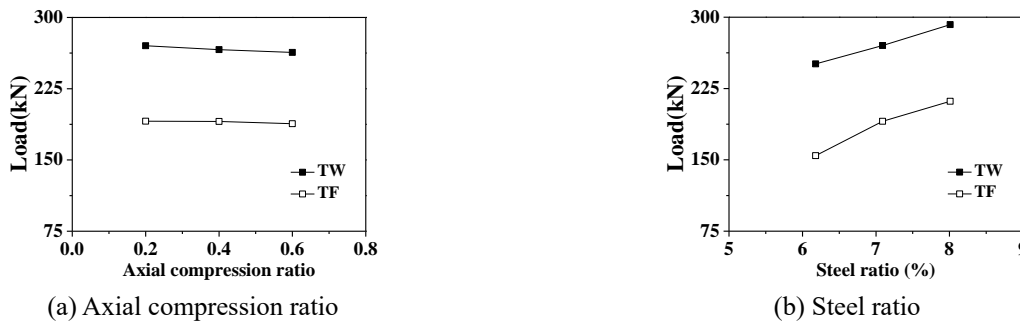


Fig. 17 Influence of design parameters on the ultimate loads

which provides little contribution to the bearing capacity, is larger than that for specimen TW.

3.4 Characteristic displacements and ductility factor

Characteristic displacements, including yield displacements Δ_y , ultimate displacements Δ_u and failure displacements Δ_f , are presented in Table 3. The ductility factors μ , which can be expressed as the ratio of the failure displacement to the yield displacement, are also presented in Table 3. The influences of design parameters on the columns' average ductility factors in the pull and push directions are shown in Fig. 18. Based on Table 3 and Fig. 18, the following observations can be made:

(1) All the ductility factors of the columns were larger than 3.5 and the average value of specimens TW and specimens TF were 4.58 and 5.88, respectively. Both values indicate good seismic performance of the SRC T-shaped columns.

(2) For the columns under the same loading angle and steel ratio, with the axial compression ratio from 0.2 to 0.6, a continuous reduction was observed for the average ductility factors. This indicates that the plastic deformation capacity of the SRC T-shaped columns deteriorated as the axial compression ratio increased.

(3) For the columns subjected to the same loading angle and axial compression ratio, as the steel ratio increased, the average ductility factors decreased at first and then increased for specimens TW, and increased slightly for specimens TF. However, the average ductility factors were similar for specimens TW and specimens TF, respectively. This indicates that the steel ratio from 6.18% to 8.01% did

not influence the ductility of the SRC T-shaped columns obviously.

(4) For the columns with the same axial compression ratio and steel ratio, the average ductility factor of specimen TF was larger than that of specimen TW. The difference is due to the fact that for specimen TF, the steel on both sides of the flange yielded in tension and compression when the column failed, and both ends of the column had obvious plastic deformation. For specimen TW, the steel on the flange yielded in tension and did not yield in compression when the column failed, and though the steel on the web yielded in tension and compression, only one end of the column had significant plastic deformation.

3.5 Stiffness degradation

Fig. 19 illustrates the degradation of the secant stiffness of the columns plotted versus the lateral displacements at the top of the columns under cyclic loading. Fig. 20 shows the influence of design parameters on the columns' average initial stiffnesses in the pull and push directions. Figs. 19 and 20 together show the followings:

(1) The stiffnesses of the columns decreased dramatically after cracks appeared in the columns. As the columns entered the yield state, the stiffness decreased rapidly, but further degradation with cycling tended to be slow and show no obvious abrupt changes.

(2) For the columns subjected to the same loading angle and steel ratio, the initial stiffnesses of the columns with a higher axial compression were greater than that with a lower axial compression. However, the rate of stiffness degeneration after cracking in the columns with a higher

Table 3 Characteristic load and displacement and ductility factor of specimens

Specimen no.	Loading direction	P_y (kN)	Δ_y (mm)	P_u (kN)	Δ_u (mm)	P_f (kN)	Δ_f (mm)	μ
TW1	Push	201.50	14.18	255.52	28.55	217.19	65.79	4.64
	Pull	197.80	10.29	276.62	19.11	235.13	45.71	4.44
TW2	Push	207.04	15.01	265.70	29.66	225.85	77.56	5.17
	Pull	205.50	15.90	274.84	39.04	233.61	85.91	5.40
TW3	Push	198.50	12.31	257.51	24.50	218.88	51.38	4.17
	Pull	201.60	9.71	268.77	19.82	228.45	36.54	3.76
TW4	Push	197.50	14.54	244.59	28.58	207.90	67.56	4.65
	Pull	191.60	14.72	257.21	28.59	218.63	64.63	4.39
TW5	Push	226.70	13.66	290.15	28.09	246.63	64.24	4.70
	Pull	228.00	13.59	294.32	27.09	250.17	60.70	4.47
TF1	Push	165.37	24.73	190.74	90.02	162.13	138.25	5.59
	Pull	164.53	24.63	190.26	71.77	161.72	131.23	5.32
TF2	Push	158.19	21.53	190.81	80.19	162.20	141.81	6.58
	Pull	162.57	19.13	190.87	80.10	162.24	143.30	7.49
TF3	Push	171.08	20.15	187.77	59.64	159.60	108.04	5.36
	Pull	168.10	20.23	188.48	60.12	160.21	107.89	5.33
TF4	Push	143.21	18.97	159.33	54.02	135.43	104.18	5.49
	Pull	127.36	16.72	149.45	44.51	127.04	99.05	5.92
TF5	Push	183.08	21.38	207.02	59.95	175.97	122.24	5.72
	Pull	188.95	20.81	216.07	59.99	183.66	124.64	5.99

axial compression was greater than that with a lower axial compression.

(3) For the columns subjected to the same loading angle and axial compression ratio, as the steel ratio increased, the initial stiffnesses decreased at first and then increased for specimens TW, and increased at first and then decreased for specimens TF. However, the average initial stiffnesses of specimens TW and specimens TF were almost the same. This indicates that the influence of steel ratio from 6.18% to 8.01% on the initial stiffnesses of the SRC T-shaped columns was insignificant. After cracks appeared in the columns, the rate of stiffness degeneration of the columns with high steel ratios was slower somewhat than that with low steel ratios.

(4) For the columns subjected to the same axial compression ratio and steel ratio, the initial stiffnesses of specimens TW were much greater than that of specimens TF. The reason is that by comparison with specimens TW, large part of column section of specimens TF is near the centroid axis, which has small contribution to the initial stiffness. However, the rate of stiffness degeneration of specimens TW was also much greater than that of specimens TF after cracking in the columns.

3.6 Energy dissipation capacity

The equivalent viscous damping coefficient h_e is used to quantify the energy dissipation capacity, which reflects the seismic energy absorption ability of a structural component.

The equivalent viscous damping coefficient h_e can be written as Eq. (1).

$$h_e = \frac{1}{2\pi} \cdot \frac{S_{(ABCD A)}}{S_{(OBE+ODF)}} \quad (1)$$

where $S_{(ABCD A)}$ and $S_{(OBE+ODF)}$ represents the area of hysteretic loop $ABCD A$ and triangles OBE and ODF respectively, which are showed in Fig. 21.

Table 4 lists the equivalent viscous damping coefficients versus the different characteristic points of the columns, where h_{ey} , h_{eu} and h_{ef} correspond to the yield point, ultimate point and failure point, respectively. Fig. 22 shows the influences of the design parameters on the energy dissipation capacities of the columns. Based on Table 4 and Fig. 22, the following conclusions can be made:

(1) The energy dissipation capacity of the columns increased with increasing loading steps. When the columns failed, all the equivalent viscous damping coefficients h_{ef} were larger than 0.3 and the average value was 0.373, which indicates that the SRC T-shaped columns had good energy dissipation capacity.

(2) For the columns subjected to the same loading angle and steel ratio, the equivalent viscous damping coefficients h_{ey} , h_{eu} and h_{ef} with a higher axial compression ratio were larger for specimens TW and smaller for specimens TF.

(3) For the columns subjected to the same loading angle and axial compression ratio, with the steel ratio increasing from 6.18% to 8.01%, the equivalent viscous damping



Fig. 18 Influence of design parameters on the ductility factors

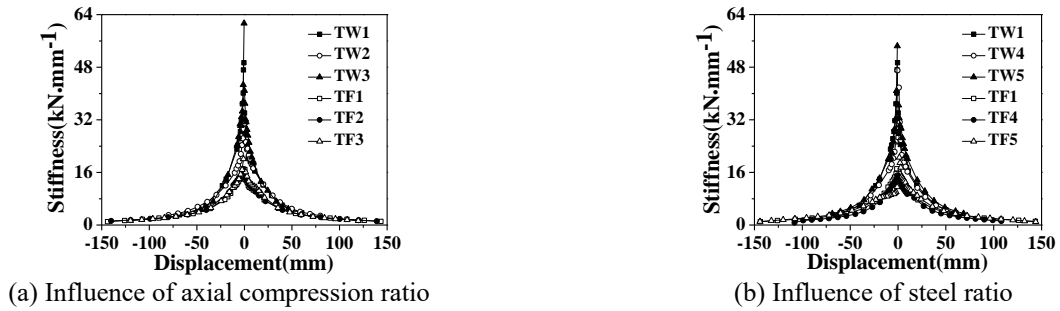


Fig. 19 Stiffness degradation

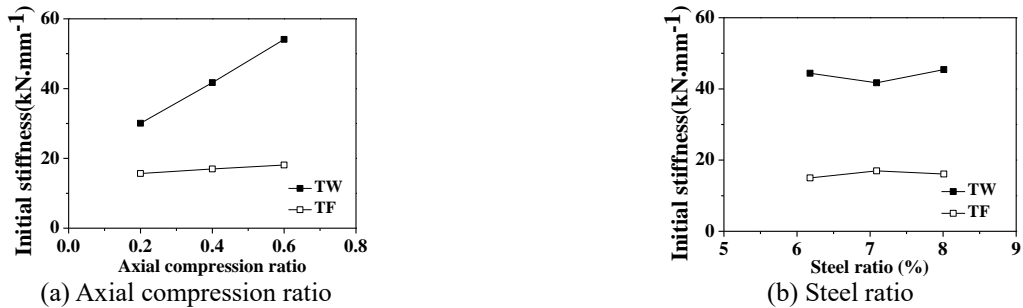


Fig. 20 Influence of design parameters on the initial stiffnesses

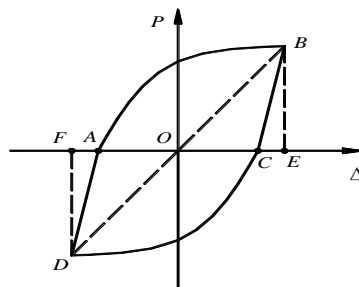


Fig. 21 Calculation of equivalent viscous damping coefficient

coefficients h_{ey} decreased at first and then increased, but the equivalent viscous damping coefficients h_{eu} and h_{ef} increased at first and then decreased.

(4) For the columns subjected to the same axial compression ratio and steel ratio, the equivalent viscous damping coefficients h_{ey} , h_{eu} and h_{ef} of specimens TF were

larger than that of specimens TW. The reason is that the steel on both sides of the flange could participate in energy dissipation completely for specimens TF, whereas only the steel on the web could dissipate energy completely for specimens TW, and the steel on the flange dissipated relatively little energy.

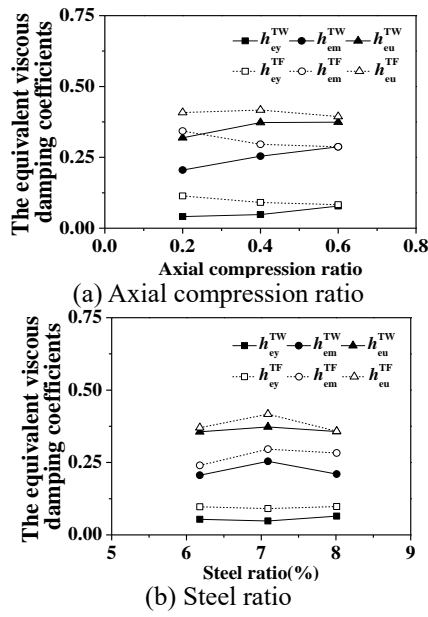


Fig. 22 Influence of design parameters on the equivalent viscous damping coefficients

Table 4 The equivalent viscous damping coefficients of specimens

Specimen no.	h_{ey}	h_{eu}	h_{ef}
TW1	0.048	0.254	0.373
TW2	0.041	0.205	0.319
TW3	0.078	0.287	0.374
TW4	0.054	0.206	0.356
TW5	0.065	0.210	0.357
TF1	0.091	0.296	0.417
TF2	0.114	0.343	0.408
TF3	0.083	0.287	0.394
TF4	0.097	0.240	0.370
TF5	0.098	0.283	0.358

4. Calculation of effective stiffness

The main mechanisms contributing to the lateral deformation of the SRC T-shaped columns are flexural and shear deformations. Therefore, both the effective flexural and shear stiffness contribute to the effective stiffness of the column, as shown in Eq. (2).

$$\frac{1}{k_e} = \frac{1}{k_{ef}} + \frac{1}{k_{es}} \quad (2)$$

where k_e , k_{ef} and k_{es} are the effective stiffness, effective flexural stiffness and effective shear stiffness of the column, respectively.

Based on the force diagram as shown in Fig. 9, the effective flexural stiffness can be calculated as Eq. (3).

$$k_{ef} = \frac{12(EI)_e}{L^3} \quad (3)$$

where L is the height of the column; $(EI)_e$ is the effective flexural stiffness of the column section, which can be derived using the reduction factor as Eq. (4).

$$(EI)_e = \beta(E_c I_c + E_s I_s) \quad (4)$$

where E_c is the elastic modulus of concrete; I_c is the moment of inertia of concrete; E_s is the elastic modulus of steel; I_s is the moment of inertia of steel; β is a reduction factor.

The effective shear stiffness can be calculated as Eq. (5).

$$k_{es} = \frac{(GA)_e}{\gamma L} \quad (5)$$

where γ is the shear stress non-uniform coefficient, taken for T-shaped section as $\gamma=1$ (Park and Paulay 1975); $(GA)_e$ is the effective shear stiffness of the column section, which can be expressed as Eq. (6).

$$(GA)_e = G_{ec} A_{ec} + G_{es} A_{es} \quad (6)$$

where G_{ec} is the effective shear modulus of concrete, which can be one half the elastic value due to the concrete cracking, namely $G_{ec}=G_c/2=E_c/4.8$ (Elwood and Eberhard 2009); G_c is the elastic shear modulus of concrete; A_{ec} is the effective shear area of concrete within the column section, for the SRC T-shaped column displaced along web, A_{ec} is the shadowed area in Fig. 23(a), and for the SRC T-shaped column displaced along flange, A_{ec} is the shadowed area in Fig. 23(b); G_{es} is the effective shear modulus of steel, which is taken as the elastic value because there is no shear yielding on steel, $G_{es}=G_s/2=E_s/2.4$; G_s is the elastic shear modulus of steel; A_{es} is the effective shear area of steel within the column section, for the SRC T-shaped column displaced along web, A_{es} can be the shadowed area in Fig. 24(a), and for the SRC T-shaped column displaced along flange, A_{es} can be the shadowed area in Fig. 24(b).

By introducing Eqs. (3)-(6) into Eq. (2), k_e can be expressed as Eq. (7).

$$k_e = \frac{1}{\frac{L^3}{12\beta(E_c I_c + E_s I_s)} + \frac{\gamma L}{G_{ec} A_{ec} + G_{es} A_{es}}} \quad (7)$$

It can be seen from Eq. (7) that β is the only undetermined factor, and it can be obtained by back-calculation from the test results.

The effective stiffness of the column can be defined based on the measured force-displacement skeleton curve with an effective force equal to $0.8P_u$ (Elwood and Eberhard 2009). Therefore, the test value of effective stiffness ($k_{e,t}$) for the SRC T-shaped columns can be obtained, as shown in Table 5.

By substituting k_e with $k_{e,t}$ in Eq. (7), the test value of β (β_t) can be obtained, as shown in Table 5. Through correlation analysis and regression fitting (Nie *et al.* 2014), β can be expressed as Eq. (8).



Fig. 23 The effective shear area of concrete within the section of SRC T-shaped column



Fig. 24 The effective shear area of steel within the section of SRC T-shaped column

Table5 Comparison on test results and calculated results of k_e

Specimen no.	Loading direction	$k_{e,t}$ (kN/mm)	β_t	$k_{e,cal}$ (kN/mm)	$k_{e,cal} / k_{e,t}$
TW1	Push	14.05	0.156	14.41	1.025
	Pull	16.69	0.187	14.41	0.863
TW2	Push	13.60	0.150	12.73	0.936
	Pull	12.51	0.137	12.73	1.018
TW3	Push	15.27	0.170	16.68	1.092
	Pull	18.41	0.208	16.68	0.906
TW4	Push	13.04	0.150	13.80	1.058
	Pull	13.37	0.155	13.80	1.032
TW5	Push	16.10	0.172	14.99	0.931
	Pull	16.36	0.175	14.99	0.916
TF1	Push	9.23	0.159	9.29	1.006
	Pull	8.24	0.141	9.29	1.127
TF2	Push	7.70	0.131	8.19	1.063
	Pull	10.58	0.183	8.19	0.774
TF3	Push	10.90	0.189	10.80	0.991
	Pull	10.46	0.181	10.80	1.032
TF4	Push	9.12	0.167	8.74	0.958
	Pull	9.23	0.169	8.74	0.947
TF5	Push	9.56	0.156	9.80	1.025
	Pull	7.89	0.127	9.80	1.242

$$\beta = 0.16(0.8 + 0.26n + 0.59n^2) \quad (8)$$

where n is the axial compression ratio of the column.

By introducing Eq. (8) into Eq.(7), the effective stiffness of SRC T-shaped column can be calculated by Eq. (9).

$$k_e = \frac{1}{\frac{L^3}{1.92(0.8 + 0.26n + 0.59n^2)(E_c I_c + E_s I_s)} + \frac{\gamma L}{G_{ec} A_{ec} + G_{es} A_{es}}} \quad (9)$$

The test results and calculated results ($k_{e,cal}$) based on Eq. (9) are compared in Table 5. The average of the ratio of

calculated results to test results of k_e is 0.997, and the standard deviation is 0.098. This result indicates that the proposed formula can assess the effective stiffness of the SRC T-shaped column with a satisfactory level of accuracy. However, it should be noted that the proposed formula is only suitable for the SRC T-shaped column with shear span larger than 2.0, on which the flexural failure usually occurs under lateral loads.

5. Conclusions

The seismic behavior of the ten SRC T-shaped columns were tested and investigated in detail under lateral cyclic loads. The following conclusions can be made based on the test and analysis:

- The failure patterns of all the investigated SRC T-shaped columns can be classified as flexural failure. However, the columns with different loading angles behaved differently in terms of the failure pattern.
- The axial compression ratio had no obvious influence on the bearing capacity of the columns, but the ductility decreased and the initial stiffness increased as the axial compression ratio increased. The bearing capacity of the columns increased as the steel ratio increased, while the ductility and the initial stiffness changed insignificantly. In addition, the columns displaced along web had higher bearing capacity and initial stiffness, but worse ductility and energy dissipation capacity than that displaced along flange.
- SRC T-shaped columns have good ductility and strong energy dissipation capacity, indicating that SRC T-shaped columns are capable of resisting an earthquake and it is feasible to employ SRC T-shaped columns in the practice of civil engineering.
- A formula was proposed to calculate the effective stiffness of SRC T-shaped column. The calculated results based on the proposed formula agreed well with the experimental results. However, further investigations must be carried out to verify the effectiveness of the formula.

Acknowledgements

The research was funded by National Natural Science Foundation of China PR (No. 51308444), Shaanxi Innovation Capacity Support Programs (No. 2019TD-029 and No.2019KJXX-018), Scientific research project of Shaanxi Education Department (No.17JS163) and Science Foundation of Henan University of Technology (No.2019BS048), which are gratefully acknowledged.

References

Abo-Zai, L., Hassan, A. and Abdel-Hafez, L.M. (2019), "Repairing post-heated L-shaped RC columns with advanced thin concrete jacketing", *Constr. Build. Mater.*, **44**(2), 212-218. <https://doi.org/10.1016/j.conbuildmat.2019.06.101>.

Chen, Z.P., Xu, J.J., Chen, Y.L. and Xue, J.Y. (2016), "Axial

compression ratio limit values for steel reinforced concrete (SRC) special-shaped columns", *Steel Compos. Struct.*, **20**(2), 295-316. <https://doi.org/10.12989/scs.2016.20.2.295>.

Elwood, K.J. and Eberhard, M.O. (2009), "Effective stiffness of reinforced concrete columns", *ACI Struct. J.*, **106**(4), 476-484. <https://doi.org/10.14359/56613>.

Hsu, T.C. (1989), "T-shaped reinforced concrete members under biaxial bending and axial compression", *ACI Struct. J.*, **86**(4), 460-468. <https://doi.org/10.14359/2967>.

Kara, I.F., Ashour, A.F. and Koroglu, M.A. (2015), "Flexural behavior of hybrid FRP/steel reinforced concrete beams", *Compos. Struct.*, **129**, 111-121. <https://doi.org/10.1016/j.compstruct.2015.03.073>.

Kim, H.G., Kim, H.M. and Kim, S.D. (2012), "Axial behavior and strength of yLC composite columns", *Adv. Struct. Eng.*, **15**(12), 2113-2130. <https://doi.org/10.1260/1369-4332.15.12.2113>.

Kim, C.S., Park, H.G., Chung, K.S. and Choi, I.R. (2014), "Eccentric axial load capacity of high-strength steel-concrete composite columns of various sectional shapes", *J. Struct. Eng.*, **140**(4), 04013091. [https://doi.org/10.1061/\(ASCE\)ST.1943-541X.0000879](https://doi.org/10.1061/(ASCE)ST.1943-541X.0000879).

Li, J., Wu, J.Y., Zhou, D.Y. and Nie L.P. (2002), "Experimental research on wide flange specially shaped section columns subjected to cyclic loading", *J. Build. Struct.*, **23**(1), 9-14. (in Chinese) <https://doi.org/10.14006/j.jzjgxb.2002.01.002>.

Liu, Z.Q., Xue, J.Y. and Zhao, H.T. (2016), "Seismic behavior of steel reinforced concrete special-shaped column-beam joints", *Earthq. Struct.*, **11**(4), 665-680. <https://doi.org/10.12989/eas.2016.11.4.665>.

Lai, B.L., Liew, J.Y.R. and Xiong, M.X. (2019), "Experimental and analytical investigation of composite columns made of high strength steel and high strength concrete", *Steel Compos. Struct.*, **33**(1), 899-911. <https://doi.org/10.12989/scs.2019.33.1.899>.

Montava, I., Irlles, R., Pomares, J.C. and Gonzalez, A. (2019), "Experimental study of steel reinforced concrete (SRC) joints", *Appl. Sciences-Basel*, **9**(8), 1528. <https://doi.org/10.3390/app9081528>.

Nzabonimpa J.D. and Hong W.K. (2019), "Experimental investigation of hybrid mechanical joints for L-shaped columns replacing conventional grouted sleeve connections", *Eng. Struct.*, **185**, 243-277. <https://doi.org/10.1016/j.engstruct.2019.01.123>.

Nie, J.G., Ma, X.W., Tao, M.X., Fan, J.S. and Bu, F.M. (2014), "Effective stiffness of composite shear wall with double plates and filled concrete", *J. Constr. Steel Res.*, **99**, 140-148. <https://doi.org/10.1016/j.jcsr.2014.04.001>.

Pham, T.P. and Li, B. (2015), "Seismic performance assessment of L-shaped reinforced concrete columns", *ACI Struct. J.*, **112**(6), 667-678. <https://doi.org/10.1061/9780784412848.146>.

Patton, M.L. and Singh, K.D. (2017), "Buckling of fixed-ended concrete-filled steel columns under axial compression", *Int. J. Steel Struct.*, **17**(3), 1059-1071. <https://doi.org/10.1007/s13296-017-9016-7>.

Park, R. and Paulay, T. (1975), *Reinforced concrete structures*, John Wiley and Sons, New York, NY, USA.

Ramamurthy, L.N. and Khan, A.H. (1983), "L-shaped column design for biaxial eccentricity", *J. Struct. Eng.*, **109**(8), 1903-1917. [https://doi.org/10.1061/\(asce\)0733-9445\(1983\)109:8\(1903\)](https://doi.org/10.1061/(asce)0733-9445(1983)109:8(1903)).

Tsao, W.H. and Hsu, C.T.T. (1993), "A nonlinear computer analysis of biaxially loaded L-shaped slender reinforced concrete columns", *Comput. Struct.*, **49**(4), 579-588. [https://doi.org/10.1016/0045-7949\(93\)90062-I](https://doi.org/10.1016/0045-7949(93)90062-I).

Tokgoz, S. and Dundar, C. (2012), "Test of eccentrically loaded L-shaped section steel fibre high strength reinforced concrete and composite columns", *Eng. Struct.*, **38**(5), 134-141. <https://doi.org/10.1016/j.engstruct.2012.01.009>.

Xiao, J.Z., Li, J. and Chen, J. (2011), "Experimental study on the seismic response of braced reinforced concrete frame with irregular columns", *Earthq. Eng. Eng. Vib.*, **10**(4), 487-494. <https://doi.org/10.1007/s11803-011-0083-z>.

CC